An investigation of the effect of aspect and compression ratios on sediment dispersion using discrete element modelling

Dong Wang, and Danielle S. Tan

Citation: AIP Advances **7**, 125227 (2017); doi: 10.1063/1.4996943
View online: https://doi.org/10.1063/1.4996943
View Table of Contents: http://aip.scitation.org/toc/adv/7/12
Published by the American Institute of Physics

An investigation of the effect of aspect and compression ratios on sediment dispersion using discrete element modelling

Dong Wang[a] and Danielle S. Tan[b]
Dept. of Mechanical Engineering, National University of Singapore, Singapore 117575

(Received 20 July 2017; accepted 14 December 2017; published online 26 December 2017)

We use discrete element modelling to simulate a system of sand being released underwater, similar to the process of releasing sediment tailings back into the sea in nodule harvesting, in 2D. The force model includes concentration-dependent drag, buoyancy, 'added mass' and Stokeslet disturbance. For a fixed number of uniform-sized particles, we vary the aspect ratio and the compression ratio of the rectangular mass of granular media pre-release. We observed that the spreading leads to a nonlinear increase with aspect ratio. On the other hand, when the compression ratio is increased, the total spreading increases; however the spread of the bulk of the sand decreases at small aspect ratios and increases at large aspect ratios. We proposed a simple theoretical model for the horizontal spreading which depends on both the aspect and compression ratios. https://doi.org/10.1063/1.4996943

I. INTRODUCTION

In today's world, electronics and electricity-based systems are ubiquitous and becoming an increasingly irreplaceable part of our society. For instance, the internet and our devices which are linked to it - mobile phones, tablets, laptops, security systems, all of these require the building and support of a vast cyber network, which cannot exist without network cables. In turn, a large amount of metal is required to build these cables. One source of such metals is the seabed, where nodules of metals such as manganese and cobalt can be found.[1–4]

The process of collecting these metals from the seabed is known as nodule harvesting.[1–5] Slurry (consisting of sediment, sand, gravels and nodules) is collected by a nodule harvester, and transported up vertically via a flexible connection system to a vertical riser, which is in turn connected to a surface mining platform. The slurry is processed on land, retaining the nodules, and the remaining material (tailings) is returned to the seabed. This is accomplished by discharging the tailings at a pre-determined depth in the sea.

This process of harvesting and discharging creates sedimentary plumes from both the nodule harvester as well as the tailing pipes. In general, the sediment tailings are composed of suspended particles of various shapes and sizes, from bentonic clay and silt (sub-microns) to sand and gravel (centimetres). Due to its particulate nature, the cloud of sediment may spread over a considerable area from the harvesting site and will take a significant amount of time to re-settle on the seabed. Rolinski et al.[6] states that typical nodule harvesting operations may disturb up to 50,000 tonnes of sediment daily, and a re-settling of 90%-95% of the sediment may take 3 to 14 years.

Unfortunately, nodule harvesting can have detrimental effects of the subsea ecosystem.[7–11] For instance, there will be an extended period of time during which the sea water is clouded (while the

[a]wangdongntu@gmail.com
[b]Corresponding author: mpetds@nus.edu.sg

tailings are re-settling), which represents a major change in the water composition. Other impacts of nodule harvesting were presented by Thiel and Tiefsee-Umweltschutz[2] in their investigation of the seabed and near-bottom water layer.

Several models have been proposed before to study the settling process of a cloud of granular material.[6,12–14] Suspended matter concentration in deep sea mining was simulated in Ref. 12 using a combination of the Hamburg large-scale geostrophic ocean model and the Lagrangian transport model. Rolinski et al.[6] improved on that model by incorporating a grain-size distribution as well as scavenging processes. Periánez[14] developed another model incorporating baroclinic terms, advection/diffusion of particles, settling and deposition. However, none of these models took into account the discrete, particulate nature of the sediment and its interaction with the surrounding fluid flow.

In this paper, we seek to understand whether compaction of the tailings before discharge will have an effect on the dispersion and re-settling process; in particular whether the bulk geometrical characteristics like the level of compaction prior to discharge, as well as the aspect ratio of the compacted solid have any significant effect. If the compacted material were released in a purely gaseous medium, it would be an elementary question. It is because the compacted material will be released underwater, and is thus subject to complex solid-fluid interaction, that makes this less straightforward. We will investigate this topic using the Discrete Element Method (DEM).

DEM, a particle-based numerical method first proposed in 1979 by Cundall and Strack,[15] focuses on the particle level (i.e. the microscale). The backbone of the simulation is the interaction between neighbouring particles, for instance the repulsion due to being in contact, as well as friction. This also includes the influence of the fluid on individual particles such as viscous drag and 'added mass'. For DEM, it is the *particle* properties (stiffness, elastic modulus, shape, size, density etc.) in addition to particle-level interactions that are of great significance, rather than assumptions made regarding the bulk (macroscale) characteristics.

Here, we model a collection of granular material, with different compression and aspect ratios, released at a short distance above a flat base in a quiescent fluid. The force model employed is from our earlier work,[16] which incorporates the effect of the local volume fraction on the drag force, the 'added mass' effect, as well as the hydrodynamic effect of neighbouring particles. The numerical simulation was validated in that work and hence the validation will not be repeated here.

This paper is laid out as follows: section II contains details regarding the numerical simulations - a brief description of the setup and boundary conditions, and an outline of the force model; the numerical simulation results are described in section III. Our simple theoretical model is outlined in section IV. Finally we conclude the paper with a brief discussion of the overall findings in section V.

II. NUMERICAL SIMULATION

A. Discrete element method (DEM) details

Although our numerical simulations are of a fluid-solid system, we only do a one-way coupling. That is, we model the solid particles and the effects of the fluid on the solids explicitly, but not vice versa. However we do consider the effect that a large concentration of solids have on the local fluid velocity, as that is integral to fluid forces like drag.

The motion of each particle i is governed by Newton's 2nd Law of Motion:

$$m_i \frac{dv_i}{dt} = \sum_{j=1}^{N} \mathbf{F}_{ij}^c + \mathbf{F}_i^d + \mathbf{F}_i^b + \mathbf{F}_i^m + \mathbf{F}_i^g, \tag{1}$$

where m_i and v_i are the mass and velocity of the i-th particle, $\mathbf{F}_{ij}^c$ is the contact force exerted by the j-th particle on the i-th particle, and $\mathbf{F}_i^d$, $\mathbf{F}_i^b$, $\mathbf{F}_i^m$ and $\mathbf{F}_i^g$ are the drag force, buoyancy force, 'added mass' force, and gravitational force respectively.

At each timestep of the simulation, the information on any one particle's position and velocity relative to its neighbours (which may or may not be in contact) is used to calculate the total force it experiences. Newton's Laws then relate the resultant force and torque to the particle's acceleration,

which we can integrate successively to obtain new values for its position and velocity. Performing this for all particles at that time-step results in an updated set of position and velocity information. We repeat this procedure for a series of small time-steps, allowing the simulation to progress forward in time.

As mentioned in the introduction, our specific choice of force model arises from our previous work,[16] in which we modeled the same system here, using a number of popular fluid force models used for solid-fluid systems. Comparison to a simple physical experiment – releasing a small container of approximately uniform-sized sand underwater – showed that the force model which reproduced all the salient qualitative behaviour of the physical experiment is one which included concentration-dependent drag forces, buoyancy, 'added mass' and Stokeslet disturbances. As this force model was chosen because of its similarity to a physical experiment, we do not include any additional validation here. The following subsections give greater detail on each of the force components in our force model.

1. Contact force

For our DEM simulations in this paper, we employ the soft-sphere contact force model (similar to that used in Ref. 17) to determine $\mathbf{F}_{ij}^{c}$. Specifically, the particles are assumed 'soft' enough that they undergo some amount of deformation when they are in contact with each other, which is quantified by a vector δ which has components both normal and tangential to the direction of contact. From Hertzian contact theory, the relationship between the deformation (overlap) is related to the repulsive force between contacting particles as follows:

$$\mathbf{F}_n = -k_n \delta_n^{1/2}\, \mathbf{n}_{ij} - \gamma_n \delta_n^{1/4} \dot{\boldsymbol{\delta}}_n \tag{2}$$

and

$$\mathbf{F}_t = \min\{-k_t \delta_n^{1/2} \boldsymbol{\delta}_t - \gamma_t \delta_n^{1/4} \dot{\boldsymbol{\delta}}_t,\ \mu^c \mathbf{F}_n\}\,. \tag{3}$$

$\mathbf{F}_n$ and $\mathbf{F}_t$ are the normal and tangential components of $\mathbf{F}_{ij}^{c}$, the force exerted by particle j on a particle i that it is in contact with. k_n, k_t, γ_n and γ_t are the stiffness and viscoelastic damping coefficients in the normal and tangential directions respectively, which are related to the particles' material properties (see Table I). $\boldsymbol{\delta}_n$ and $\boldsymbol{\delta}_t$ are the normal and tangential components of the overlap vector (dots overhead denote rate of change with time), n_{ij} is the unit vector acting along the line from the centre of particle j to the centre of particle i, and μ^c is the material friction coefficient.

2. Drag force

For the drag force $\mathbf{F}_i^d$, we use Di Felice[18]'s drag force model which explicitly takes the local solid volume fraction ϕ into account:

$$\mathbf{F}_i^d = \mathbf{F}_{i,0}^d\, g(\varepsilon) = -C_d \frac{\rho_f \left|(\mathbf{v}_i - \mathbf{u}_i^f)\right| (\mathbf{v}_i - \mathbf{u}_i^f)}{2} \frac{\pi d^2}{4} \varepsilon^{-\beta}, \tag{4}$$

TABLE I. Formulae for calculating stiffness and damping coefficients in terms of radius R, mass m, Young's modulus E and Poisson's ratio ν of a contacting pair of particles, each represented by subscripts i and j.

Variable	Formulae
k_n	$(4/3)\sqrt{R_{\text{eff}}}E_{\text{eff}}$
k_t	$8\sqrt{R_{\text{eff}}}G_{\text{eff}}$
γ_n	$\alpha\sqrt{m_{\text{eff}}k_n}$
γ_t	$\alpha\sqrt{m_{\text{eff}}k_t}$
R_{eff}	$(1/R_i + 1/R_j)^{-1}$
E_{eff}	$\left[(1-\nu_i^2)/E_i + (1-\nu_j^2)/E_j\right]^{-1}$
G_{eff}	$\left[2(1+\nu_i)(2-\nu_i)/E_i + 2(1+\nu_j)(2-\nu_j)/E_j\right]^{-1}$
m_{eff}	$(1/m_i + 1/m_j)^{-1}$

$g(\varepsilon) = \varepsilon^{-\beta}$ is a 'weight' added to the more well-known (concentration-independent) expression for drag. ρ_f is the fluid density, d is the particle diameter, $\mathbf{v}_i$ is the velocity of the i-th particle, and $\mathbf{u}_i^f$ is the fluid velocity at $\mathbf{x}_i$. The drag coefficient C_d is given as:

$$C_d = (0.63 + \frac{4.8}{\sqrt{\mathrm{Re}}}), \tag{5}$$

where the particle Reynolds number is:

$$\mathrm{Re} = \frac{\rho_f d\,|\mathbf{v}_i|}{\mu}, \tag{6}$$

μ is the dynamic viscosity of fluid and ε is the local void fraction whose exponent is defined as:

$$\beta = 3.7 - 0.65 \exp\left[-\frac{(1.5 - \log(\mathrm{Re}))^2}{2}\right]. \tag{7}$$

For a single particle the local void fraction (and hence $g(\varepsilon)$) approaches one, reducing the drag force back to the well-known hydrodynamic drag expression. Inversely, as the local solid fraction (the concentration) increases and the void fraction decreases (because the concentration and the void fraction sum to one), $g(\varepsilon)$ increases exponentially.

3. Buoyancy

The buoyancy $\mathbf{F}_i^b$ is expressed as follows:

$$\mathbf{F}^b = -\frac{1}{6}\pi\rho_f d^3 \mathbf{g}, \tag{8}$$

where $\mathbf{g}$ is the gravitational acceleration.

4. Added mass effect

We include an 'added mass' as part of the fluid effects term, to model the resistance experienced by the particle when accelerating the fluid in its immediate surroundings, which is commonly used in numerical simulations of solid-fluid systems.[19–22] This added mass component is usually incorporated into the governing equation on the left hand side, written as:

$$(m_i + C_m m_f)\frac{dv_i}{dt} = \sum_{j=1}^{N} \mathbf{F}_{ij}^c + \mathbf{F}^d + \mathbf{F}^b + \mathbf{F}_i^g. \tag{9}$$

This expands to:

$$(m_i + C_m m_f)\frac{dv_i}{dt} = \sum_{j=1}^{N} \mathbf{F}_{ij}^c - \frac{1}{2}C_d\rho_f\,|(\mathbf{v}_i - \mathbf{u}_i)|\,(\mathbf{v}_i - \mathbf{u}_i)\frac{\pi d^2}{4}\varepsilon^{-\beta} + \frac{\pi d^3}{6}(\rho_f - \rho)\mathbf{g}, \tag{10}$$

where C_m is the added mass coefficient and the accelerated fluid mass is $m_f = \rho_f \left(\pi d^3\right)/6$. Here we use $C_m = 0.5$, which means the particle mass was increased by 20% to account for the fluid mass.[19,20] As shown in a previous study,[16] incorporating the added mass effect does not significantly change the fluid-solid interaction qualitatively, but it does increase the model's quantitative accuracy. It may not be seen as particularly significant, as the size of each particle is relatively small – and therefore the amount of 'added mass' due to displacing fluid ahead of the particle's motion is also, logically, small. Given our interest in the settling time of the cluster of particles, however, we cannot simply neglect this resistive force.

5. Stokeslet disturbance

Just as moving fluid will affect a group of particles in close proximity, so too will a moving group of particles each have some effect on the fluid velocity at some nearby position. We are particularly interested in this when the position of interest coincides with that of a solid particle – in other words, when the motion of neighbours indirectly affect the motion of a single particle by influencing the fluid vicinity in its immediate vicinity. It can be argued that this effect is minimised in a sparse

system where the solid particles are very far apart; in this case where a cloud of particles are moving collectively under gravity, the effect is not insignificant. In fact, for such a group of particles falling through an originally quiescent body of fluid, the fluid motion at any point will, logically, be the collective result of all the surrounding solid particles' influence.[23,24]

We can think of a Stokeslet disturbance as the effect on the ambient fluid velocity caused by a single neighbouring particle's motion; the resultant effect due to a collection of particles is then the summation of the Stokeslet disturbances contributed by the neighbouring particles. The superposition is weighted by the proximity of the particles via the Stokeslet tensor $\mathbf{w}(\mathbf{x}_i; \mathbf{x}_j)$, such that the effect is diluted for particles further away from the point of consideration. At the centre of mass of the i-th particle $\mathbf{x}_i$, the disturbed fluid velocity $\mathbf{u}_i^f$ is approximated as:

$$\mathbf{u}_i^f = \sum_{j \neq i} \mathbf{w}(\mathbf{x}_i; \mathbf{x}_j) 3\pi\mu d(\mathbf{v}_j - \mathbf{u}_j^f), \tag{11}$$

where $\mathbf{v}_j$ is the velocity of the neighbouring j-th particle, $1 \leq j \leq N$ and $\mathbf{u}_j^f$ is the fluid velocity at $\mathbf{x}_j$ in the absence of the j-th particle, from the previous time-step. The Stokeslet tensor is given by:

$$\mathbf{w}(\mathbf{x}_i; \mathbf{x}_j) = \frac{1}{8\pi\mu}\left(\frac{\mathbf{I}}{|\mathbf{x}_i - \mathbf{x}_j|} + \frac{(\mathbf{x}_i - \mathbf{x}_j)(\mathbf{x}_i - \mathbf{x}_j)}{|\mathbf{x}_i - \mathbf{x}_j|^3}\right), \tag{12}$$

where $\mathbf{x}_j$ is the centre of mass of the j-th particle and $\mathbf{I}$ is the identity tensor. The above expression for the fluid velocity $\mathbf{u}_i^f$ is then used in the concentration-dependent drag term (Eq. 4).

Special treatment is required to model the Stokeslet disturbance contributed by the wall (this contribution is non-zero when the fluid nearby is in motion, since relative velocity is then non-zero). Here we introduce 'mirror' particles into the system – when the particles are within a specified proximity to the wall, particles are introduced on the 'other side' of the wall. These virtual particles are reflections of the actual particles in terms of size and kinematics, such that their presence will result in the mutual Stokeslet disturbances cancelling out exactly along the wall. However when the particles are too close to the wall, the Stokeslet disturbance from their reflected counterparts results in a very large repulsive force which causes the actual particles to 'bounce'. Hence, we only introduce the 'mirror' particles when the falling particles are $10d$ (0.01 m) away from the wall. The Stokeslet disturbance result from the real particles are only considered when the particles are away from the wall with the distance of $5d$ (0.005 m). A more detailed description of our implementation of the Stokeslet disturbance and 'mirror' particles can be found in Ref. 16.

B. Simulation description

Figure 1 shows the general steps in the numerical simulation. First, particles (450 spheres with the average diameter of 1 mm and density 2400 kg/m^3) are 'poured' randomly into a rectangular container with different aspect ratios. 7 values of width were used - 0.01 m, 0.016 m, 0.018 m, 0.02 m, 0.022 m, 0.03 m and 0.04 m. The particles are allowed to settle until the average kinetic energy is at a minimum. Next, a rigid wall made up of particles (2 mm diameter, density 2400 kg/m^3) is used to compress the particles by moving a prescribed displacement Δy downwards from its initial position at y_0 (Figure 1b–c). We varied the value of Δy for each aspect ratio to obtain different levels of compaction ranging from 0 to 23.8%. The particles are then allowed to resettle (Figure 1d). We consider this the initialised state of the particles.

Next, the lightly compacted particles are allowed to fall from rest through a quiescent medium with the same properties as water (density=1030 kg/m^3, viscosity=1.08×10^{-3} Pa·s) from a distance of 0.1m above the base (Figure 1e). Spheres of 2 mm diameter, fixed rigidly in space, form the rough bottom boundary in the simulation. We use D90 and D100 to denote the horizontal spreading of the particles throughout the simulation. D90 and D100 represent the diameters of the circle in which 90% and 100% of the particles falls in respectively.

The time step size for all the simulations is 5×10^{-6}s, and we calculate the local solid fraction ϕ of a particle using:

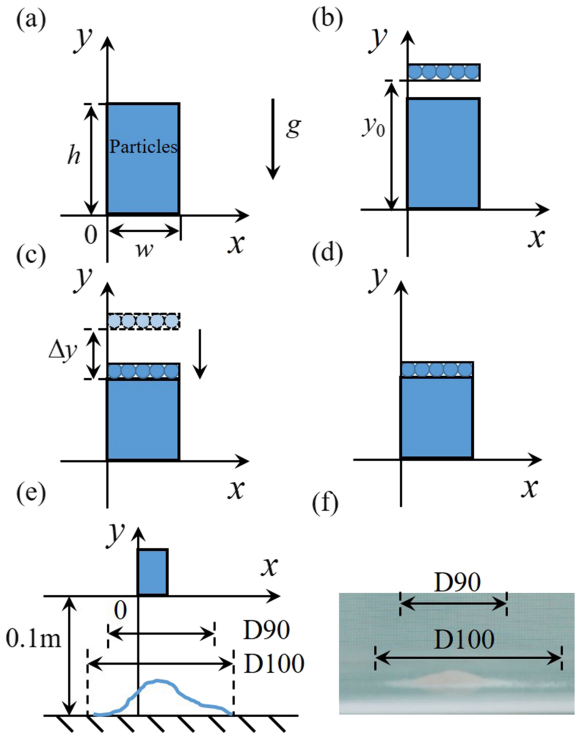

FIG. 1. Simulation procedure: (a) particles are 'poured' into a rectangular container; (b) a rigid wall made up of larger particles is introduced at height y=y_0; (c) the rigid wall moves a prescribed vertical distance to compress the mixture; (d) the mixture is allowed to resettle; (e) the compacted mixture is released at 0.1m height to re-settle on the simulation floor; (f) side view of the sand settled on the floor. D90 and D100 represent the horizontal distance over which 90% and 100% of the particles fall respectively.

$$\phi = \frac{V_P}{V_T} = \frac{n\pi d^3/6}{0.1 \times 0.1 \times 0.001}, \tag{13}$$

where V_T is the volume of a $0.1 \times 0.1 \times 0.001 m^3$ space centred at the position of interest, and V_P is the volume of the n particles whose centres fall within the borders of the space.

It must be noted that although the simulations are 3-dimensional, our simulation domain is only 1 particle diameter thick and no motion is allowed in the in-plane (z) direction. Thus the simulation results can be viewed from a 2-dimensional point of view. The results obtained are thus still representative of a 3-dimensional system; the simulation results were compared to a physical experiment in 3-dimensions in a previous work.[16]

III. RESULTS

In section III A we present the results from a set of numerical simulations where the pre-release state of the lightly-compacted granular material is varied in two ways: (1) aspect ratio of the bulk geometrical shape, and (2) the level of compaction applied before release which we represent using a compression ratio. For all of these simulations, the total number of particles is held constant, so that the total solid volume is maintained.

Both the aspect ratio and compression ratio can be defined more clearly in reference to Figure 1. Figure 1a shows the rectangular container which is filled with the granular mixture. We use the bulk geometry of the granular mixture at this point, pre-compaction, to define the aspect ratio (width w divided by height h).

The amount of compaction in the preparation is controlled by the displacement of the horizontal rigid wall shown in Figure 1b–d. Specifically, the prescribed downward vertical displacement Δy of the rigid wall controls the level of compaction the granular material is exposed to. Our compression ratio is thus defined as $[h - (y_0 - \Delta y)]/h$.

Another issue that we consider here is whether the initialisation procedure, in particular the compaction procedure, affects the dispersion and settling behaviour of the sand. We describe these results in section III B.

We quantify the spreading using two parameters - D100 and D90, which are the diameters of the circles enclosing 100% and 90% respectively of the granular particles after settling. A photograph of a typical final settling pattern, with the two circles of diameter D100 and D90, is shown in Figure 1f for clarity. For our 2D simulation, D100 and D90 are the horizontal spread covered by 100% and 90% of the particles respectively. Both measurements are centred about the horizontal midpoint of the compacted granular material ($x = w/2$).

For all the results presented here, we show the averaged values of 3 similar numerical simulations with the only difference being the initial particle configuration, and use the average particle diameter d as the normalising lengthscale.

We have observed from a separate study[25] that the size of the granular material also has some effect on the horizontal spreading. Thus we feel that the results of our work may be more useful to others studying mixtures of different or varying sizes, if we use the (average) particle as the normalising lengthscale.

A. Aspect and compression ratios

Figure 2 shows the time evolution of (a) horizontal spreading D100/d, (b) average vertical displacement $\bar{y}$, (c) average vertical velocity $\bar{V}_y$ and (d) average local solid fraction $\bar{\phi}$, for compression ratios of 0%, 7.62%, 14.6% and 21.5%. We observe that qualitatively, the simulations behave similarly regardless of compression ratio. Figure 3 shows the snapshots of these simulations at different times throughout the dispersion process. The most obvious quantitative difference is in the horizontal spreading - the simulations of more compacted material tend to reach a plateau of a higher value

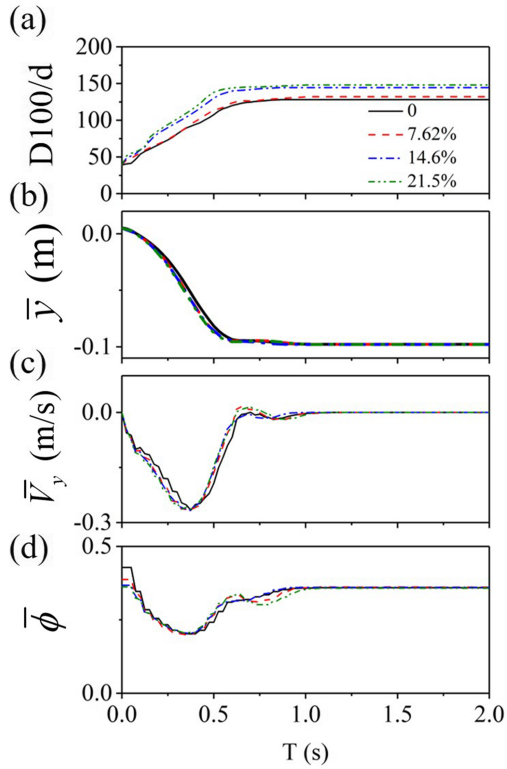

FIG. 2. Evolution of (a) horizontal spreading, (b) average vertical position, (c) average vertical velocity and (d) average local volume fraction with time for simulations with different compression ratio at 0, 7.62%, 14.6% and 21.5%. The aspect ratio is 3.57.

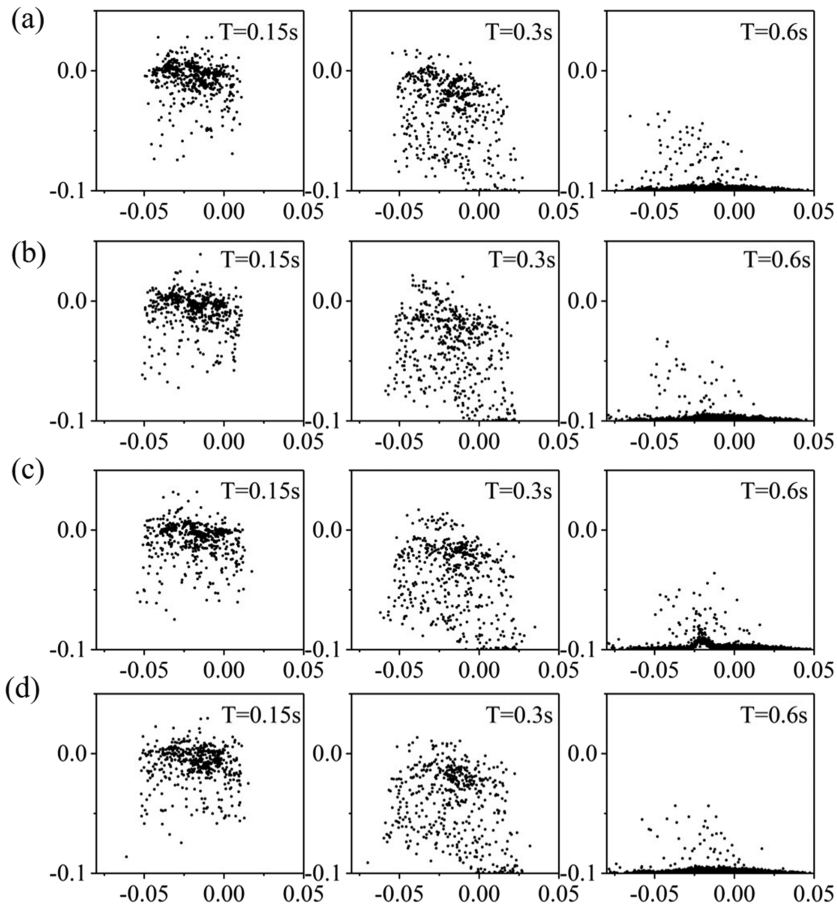

FIG. 3. Snapshots of the simulations with different compression ratios as (a) 0%, (b) 7.62%, (c) 14.6% and (d) 21.5% at increasing time interval. The aspect ratio is 3.57.

(i.e. spreads more), but at a slightly later time. It is observed that by T=0.6s, most particles have already settled, as shown by both Figs. 2 and 3. As time passes, the average vertical velocity first increases from zero to its maximum downwards value, then when particles begin reaching the bottom it gradually reduces back to zero. The average local solid fraction will initially decrease because of the motion of the particles away from their compacted state, and then reach ≈ 0.36 when all the particles settle down. As a whole, an increase in compression ratio results in greater energy stored in the compacted material, and thus particles initially accelerate faster and spread further as shown by the larger increases in both average vertical velocity and average vertical displacement, which culminates in a larger D100/d.

Figure 4 shows the time evolution of total horizontal spreading D100/*d*, average vertical displacement, average vertical velocity and average local solid fraction for three different aspect ratios (approximately 0.5, 1 and 4). Snapshots at different times for the three simulations are shown in Figure 5. It is observed that as the aspect ratio increases, the greatest downward velocity achieved decreases. This is because at higher aspect ratios, the amount of compression (and thus, increase in local solid fraction) due to the weight of the particles themselves decreases. It is thus unsurprising that among the three, the simulation with highest aspect ratio exhibits the least horizontal spreading. From Figure 5, it can be seen that at T=0.15s, the local particle fraction of the simulation with aspect ratio as 3.57 is smaller and more particles are settled down at T=0.6s.

Figure 6 shows the scatter points for D100 against compression ratio, for 7 different aspect ratios.

It can be seen that D100 is a complex function with respect to aspect ratio and compression ratio. However, some very general observations can be made about the overall trends:

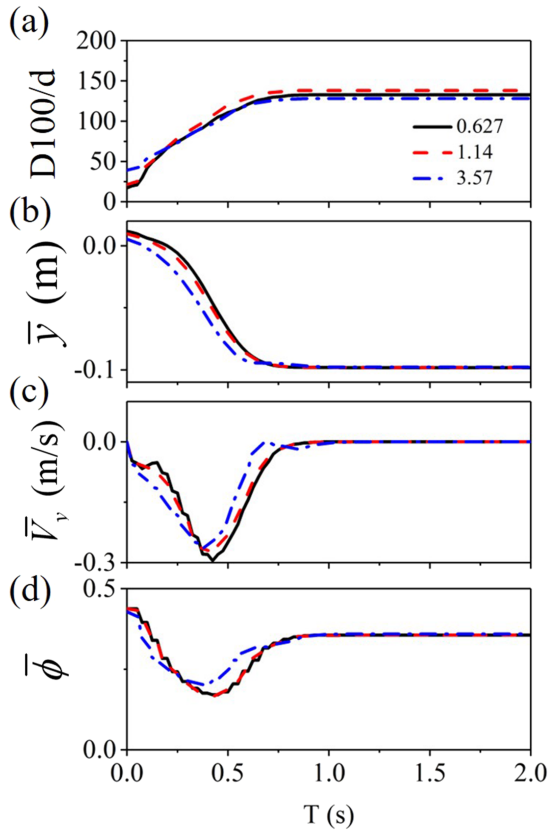

FIG. 4. Evolution of (a) horizontal spreading, (b) average vertical position (c) average vertical velocity and (d) average local volume fraction with time for simulations with different aspect ratios at 0.627, 1.14 and 3.57. The compression ratio is 0%.

- D100 generally increases with compression ratio, except for when the aspect ratio is close to 1.
- D100 tends to increase with aspect ratio, particularly when the compression ratio is above 10%.
- For aspect ratios close to 1 (0.783, 0.930 and 1.140), the behavior of D100 on compression ratio is nonlinear. This is evidenced by the correlation value R^2 being close to 0.
- At 0% compression, D100 behaves in a non-regular manner.

Except for the 3 simulated cases with aspect ratio close to 1, D100 generally increases with compression ratio. Physically this means that the area of spread increases with increasing amounts of initial compression. We find this observation not to be very surprising, as the simulated particles are generally monosized and particle-particle interactions are modelled on spring-like behaviour. If the simulated mixtures had a wider size distribution, then we expect that the greater compression would result in a greater local solid fraction rather than an increase in the elastic potential energy of the system. However the microstructure of the particle mixture is random, and thus the bulk response to compression would not be linear like an elastic solid, as stated earlier. This also means that when there is no compression applied, D100 will depend entirely on the initial configuration – thus leading to the irregular behaviour observed.

When the aspect ratio is close to 1 (the three simulation cases with aspect ratio 0.783 to 1.140), the variation in scatter is only about three particle diameters. So we feel it is reasonable to conclude that D100 is largely independent of the compression ratio when the aspect ratio is close to 1. We propose that it may be because the applied compression would not cause significant change in aspect ratio when it is already close to 1, and hence does not lead to significant difference in terms of the spreading (D100).

The values of D100 are generally larger at larger aspect ratios – i.e., the area of spread is greater when the width to height ratio of the compacted granular mixture increases. Quantitatively the difference in D100 between the two most extreme aspect ratios here is on the order of 10 mm,

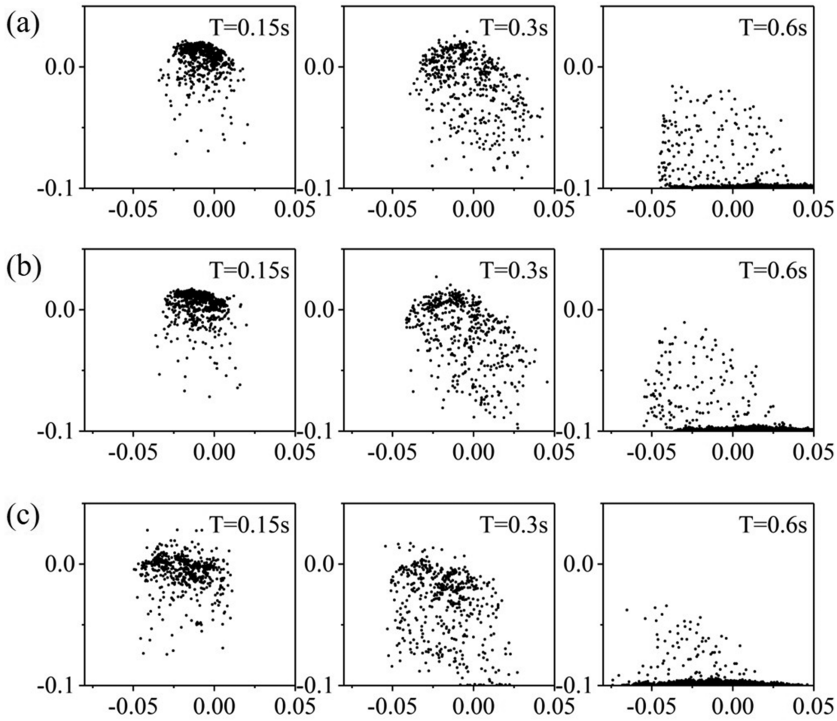

FIG. 5. Snapshots of the simulations with different aspect ratios (a) 0.627, (b) 1.14, (c) 3.57 at increasing time interval. The compression ratio is 0%.

which is 10 particle diameters, a value that is not insignificant. Again, this observation may not be surprising; intuition tells us that if we compared how two equal amounts of some substance scatter after a fall, the substance that was originally more thinly spread would fall over a wider area compared to if it had been mostly stacked up before release. What should be taken note of, however, is that the increase in horizontal spreading is not proportional to the increase in width w. This implies that the initial height h of the compacted material has some influence on the overall spreading as well.

Figure 6 showed the maximum spreading achieved, but simple physical experiments (see Figure 1f) showed that the vast majority of the particles would fall in a smaller area. Hence there is some value in looking at the corresponding results for D90 as well, as shown in Figure 7.

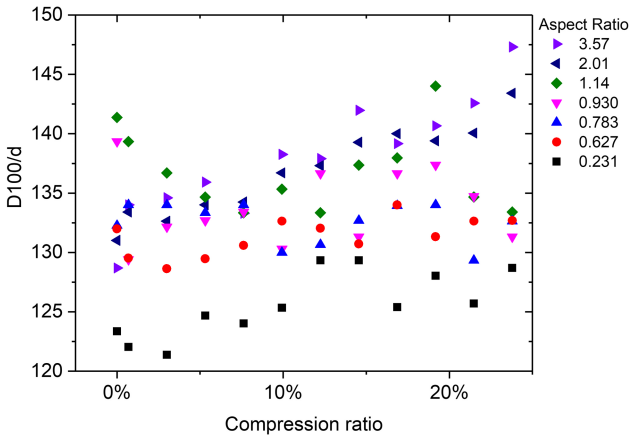

FIG. 6. Points of spreading diameter D100/d against compression ratio for different aspect ratios.

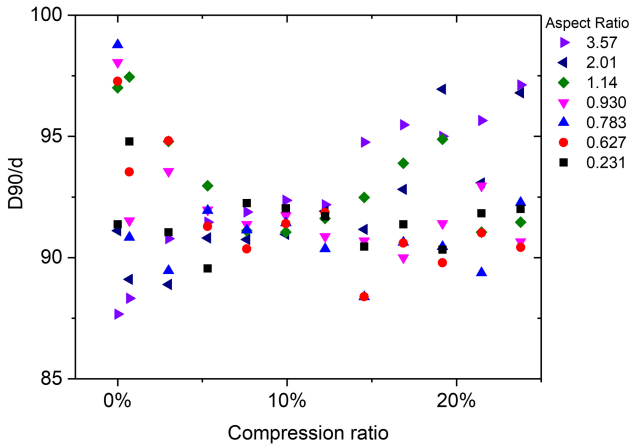

FIG. 7. Points of spreading diameter D90/d against compression ratio for different aspect ratios.

Here we observe that the general trend of increasing D90 with increasing aspect ratio still holds for compression ratios above $\approx 7\%$. However unlike for D100, D90 generally decreases with compression ratio except for the two largest aspect ratios 2.0 and 3.6. This shows that when a larger amount of compression is applied, the bulk of the particles are compacted and do not spread apart as much. The difference compared to D100 is likely due to the particles on the boundary which experience the compression directly, and build up elastic potential energy. As for the largest aspect ratio, the similar tendency to that shown in Figure 6 is likely due to the increased surface to volume ratio, in particular the number of particles on the surface that experience the compression directly.

To summarise: when the compression ratio is relatively large, both D90 and D100 increase with increasing aspect ratio. This means that a compacted material with a larger base as compared to its height will finally settle over a larger area than the same volume of material compacted into a slimmer but taller shape. The effect of compression ratio, on the other hand, is slightly more complex. Except at high aspect ratios, D90 generally decreases with increasing compression ratio; conversely, D100 increases with compression ratio except when the aspect ratio is close to 1. Physically this means that when a greater compression is applied at low aspect ratios, the bulk of the particles will settle in a smaller area but a minority will form a larger outer ring. On the other hand, if no compression is applied, the results can be unpredictable. In the context of reducing the pollution from nodule harvesting, we can conclude that the total horizontal spreading will be minimised if the sediment tailings are compacted into a shape with low aspect ratio and at a low compression ratio.

B. Effects of compaction procedure

In this section, we investigate the effect of our initialisation procedure, in particular how the compaction process affects the particle sedimentation. Including the method used to produce the results in section III A, a total of four different compaction procedures were studied:

- '1C0': Compress the particles to determined compression ratio. The particles are released underwater immediately after.
- '1C5': Compress the particles to determined compression ratio. The particles are allowed to settle in this compressed state for 5 seconds, before being released underwater.
- '1C10': Compress the particles to determined compression ratio. The particles are allowed to settle in this compressed state for 10 seconds, before being released underwater.
- '2C0': Compress the particles to determined compression ratio. Remove the wall, and then re-compress the particles again to same determined compression ratio. The particles are released underwater immediately after.

The results in section III A were produced using procedure 1C0. Here we ran three simulations with different initial particle configurations for each compaction procedure, and present the averaged

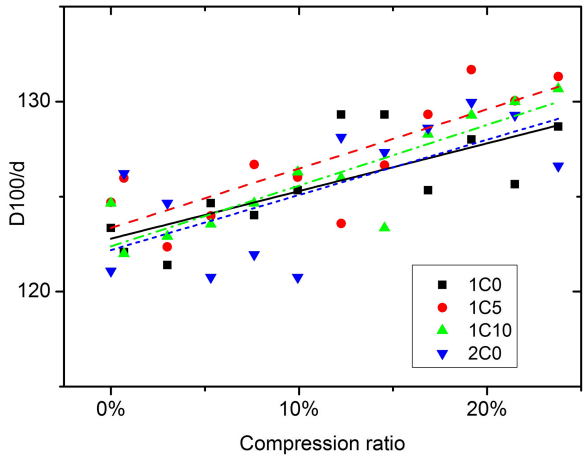

FIG. 8. Points and linear fitting lines of spreading diameter D100/d against compression ratio for different compaction procedures.

TABLE II. Linear fit parameters for D100/d versus compression ratio ϵ for different compaction procedures, where D100/$d = a_{100} + b_{100}\,\epsilon$.

Symbol	Procedure	a_{100}	b_{100}	R^2
■	1C0	123	25.2	0.512
●	1C5	123	31.2	0.643
▲	1C10	122	31.9	0.744
▼	2C0	122	29.2	0.407

results. Note that these simulations were run using the same aspect ratio of 0.231 – this is the aspect ratio which gives the lowest values of D100 (total horizontal spreading) in general, for the investigated range of compression ratios. Since this 'optimum' case is the one we recommend for reducing pollution, it makes sense to use it to study the effect of compaction procedure.

Figure 8 shows the normalised total spread D100/d as a function of compression ratio for the four different compaction procedures respectively. Linear fits are plotted also, with the fit parameters listed in Table II.

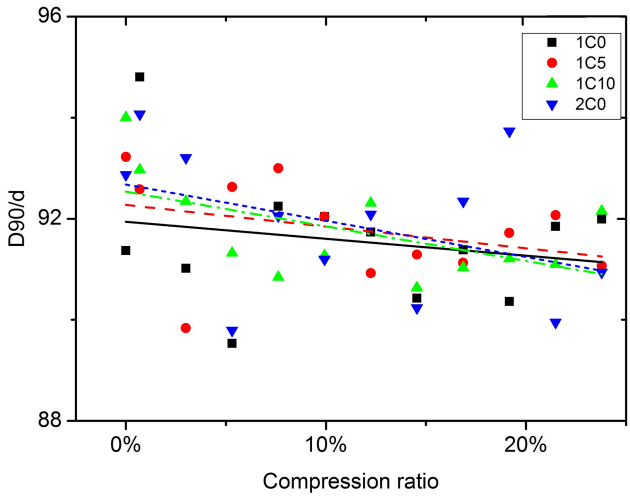

FIG. 9. Points and linear fitting lines of spreading diameter D90/d against compression ratio for different compaction procedures.

TABLE III. Linear fit parameters for D90/d versus compression ratio ϵ for different compaction procedures, where D90/$d = a_{90} + b_{90}\,\epsilon$.

Symbol	Procedure	a_{90}	b_{90}	R^2
■	1C0	91.9	-3.37	-0.0516
●	1C5	92.2	-4.25	0.0338
▲	1C10	92.5	-6.89	0.239
▼	2C0	92.7	-7.19	0.0763

From the figure, it can be observed that (1) D100 increases with compression ratio for all four compaction procedures; and (2) the linear fits for all four compaction procedures are very close. In fact there is very little difference in terms of D100 among the compaction procedures for any one compression ratio – the largest difference is approximately 4mm (4 particle diameters) only.

Considering the goodness of the linear fit (see R^2 in Table II), we can arrange the 4 procedures in terms of increasing variation from a linear relationship: 1C10 < 1C5 < 1C0 < 2C0. This means that for the numerical simulation, allowing the particles to settle for a longer period immediately after compaction can significantly reduce the deviation from a linear fit.

As with the results in section III A we consider the results for D90, representing the bulk of the spreading, plotted in Figure 9. The fit parameters for the plotted linear fits are listed in Table III.

Unlike D100 (Figure 8), D90 varies in a strongly nonlinear manner with increasing compression ratio. We can only say, very loosely, that D90 generally decreases with increasing compression ratio for all 4 compaction procedures at compression ratios less than 10%.

IV. THEORETICAL MODEL

We propose a simple theoretical model to predict the amount of horizontal spreading based on the aspect ratio and initial compression of the compacted granular media. In the context of determining the extent to which underwater dispersion affects the local ecosystem, interest lies more with D100 (total horizontal spreading) rather than D90 (the spreading of the bulk of the particles). Hence this theoretical model is, specifically, a prediction for D100.

At the moment of release from the container, the particles 'explode' within a very short period of time – the elastic energy stored during compression is released and converted to kinetic energy. Since the dispersion is taking place in quiescent fluid, there is no pre-existing velocity field. The dispersion will thus be, prior to gravitational acceleration and ignoring any Brownian motion, radially symmetrical about the centre of the compacted material. Applying this geometrical symmetry with respect to both $x-$ and $y-$coordinates, the block can be regarded as four parts with same dimensions of $\frac{1}{2}h \times \frac{1}{2}w$ (see Figure 10). Unit depth (into the page) is assumed. By assuming the block is linearly elastic,

$$4 \times \frac{1}{2}(\frac{1}{4}m)v^2 = \frac{1}{2}E_m\Delta y^2 + U_{\text{initial}}, \tag{14}$$

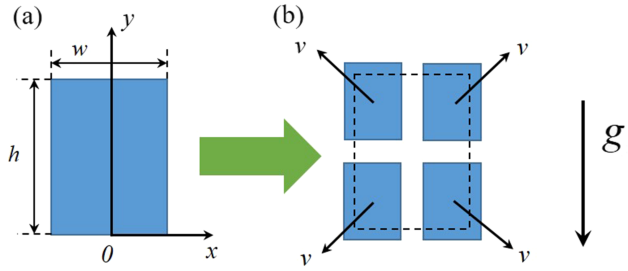

FIG. 10. Schematic of the block of granular media (a) before release and (b) after release from the container. Gravity acts in the negative y-direction.

where m and v are the mass and velocity of a section of the block, Δy is the applied displacement during the compaction of the granular material, E_m represents its compression 'stiffness' and U_{initial} represents the energy stored in the system prior to the applied compression due to the weight of the sand. Thus, $v = \sqrt{(E_m \Delta y^2 + 2U_{\text{initial}})/m}$. E_m and U_{initial} only depend on the initial shape of the bulk particles and therefore vary with different aspect ratio and initial packing, but are independent of the compression ratio. In the following derivation, we consider only the center point of the top right block with the initial velocity $v_x = v_y = \frac{1}{\sqrt{2}}v$.

In the $y-$direction, the block moves up first resulting from the initial positive v_y and then down due to the effect of gravity and drag. When moving upwards, the drag force is in the negative $y-$direction, while it is positive $y-$direction when the is block moving down. According to Newton's second law,

$$m(1 + C_m)\frac{d^2y}{dt^2} = -mg + F_y^d + F^b, \tag{15}$$

where $m = \frac{1}{4}wh\rho$, $F^b = \frac{1}{4}wh\rho_f g$, $F_y^d = -\alpha_y(\frac{dy}{dt})^2$ when the block moves up and $F_y^d = \alpha_y(\frac{dy}{dt})^2$ when the block moves down, $\alpha_y = \frac{1}{2}\rho_f C_d(\frac{1}{2}wh + h \times 1)$. Solving for vertical displacement y:

$$y(t) = \left\{ \begin{array}{ll} -\dfrac{1}{\alpha_y}(1 + C_m)\, m \ln\left[\cos\left[\dfrac{\sqrt{\alpha_y}\sqrt{F^b - mg}\,(C_1\,(1 + C_m)\, m - t)}{(1 + C_m)\, m}\right]\right] + C_2, & 0 < t < t_1 \\ \dfrac{1}{\alpha_y}(1 + C_m)\, m \ln\left[\cos\left[\dfrac{\sqrt{-\alpha_y}\sqrt{F^b - mg}\,(C_3\,(1 + C_m)\, m - (t - t_1))}{(1 + C_m)\, m}\right]\right] + C_4, & t > t_1 \end{array} \right\} \tag{16}$$

where $t_1 = C_1(1 + C_m)m$ is the time at which the block reaches its highest point and when $v_y = 0$. The boundary conditions are $y(0) = \frac{3}{4}h$, $y'(0) = \frac{1}{\sqrt{2}}v$, $y'(t_1) = 0$ and y is continuous at $t = t_1$. The coefficients are then found to be:

$$C_1 = -\frac{1}{\sqrt{\alpha_y(F^b - mg)}}\cos^{-1}\left[-\frac{\sqrt{2F^b - 2mg}}{\sqrt{2F^b - 2ng + \alpha_y v^2}}\right], \tag{17}$$

$$C_2 = C_4 = \frac{1}{4\alpha_y}\left[3\alpha_y h + 2m\,(1 + C_m)\ln\left(\frac{F^b - mg}{F^b - mg + \alpha_y v^2/2}\right)\right], \tag{18}$$

$$C_3 = 0\,. \tag{19}$$

In the horizontal direction, the drag force is always in the negative $x-$direction. According to Newton's second law,

$$m(1 + C_m)\frac{d^2x}{dt^2} = \alpha_x\left(\frac{dx}{dt}\right)^2, \tag{20}$$

where $\alpha_x = \frac{1}{2}\rho_f C_d(\frac{1}{2}wh + w)$. Using the boundary conditions $x(t = 0) = w/4$ and $\frac{dx}{dt}(t = 0) = \frac{1}{\sqrt{2}}v$, horizontal displacement x can be solved as:

$$x = -\frac{(1 + C_m)\, m \ln\left(C_5\,(1 + C_m)\, m + \alpha_x t\right)}{\alpha_x} + C_6, \tag{21}$$

where

$$C_5 = -\frac{\sqrt{2}}{v}, \tag{22}$$

$$C_6 = \frac{1}{4\alpha_x}\left[\alpha_x w + 2m\,(1 + C_m)\ln\left(2\left(\frac{m\,(1 + C_m)}{v}\right)^2\right)\right]. \tag{23}$$

The total time t_2 for the block to settle down can be obtained by setting $y(t_2) = -0.1 + \frac{1}{4}h$:

$$t_2 = t_1 + m\,(1 + C_m)\,\frac{\cos^{-1}\left[\exp\left(\frac{\alpha_y(0.25h - 0.1 - y_0)}{m(1 + C_m)}\right)\right]}{\sqrt{\alpha_y(mg - F^b)}}\,. \tag{24}$$

The horizontal spreading (D100) is thus $2x(t_2)$.

A. Empirical fitting

Using the theoretical framework outlined above, we determine values for E_m and U_{initial} such that the model gives predictions similar to the simulation results, for horizontal spreading as a function of compression ratio at different aspect ratios. Both these simulation results and the theoretical model predictions are plotted in Figure 11a. The correlation between simulation and theoretical D100/d is plotted in Figure 11b. We can see that the points all cluster on the diagonal $y = x$ line, with an average error of 1.22%, and thus conclude that the theoretical D100/d values agree reasonably well with that measured from the simulations. Figure 11c plots the comparison between theoretical and simulation

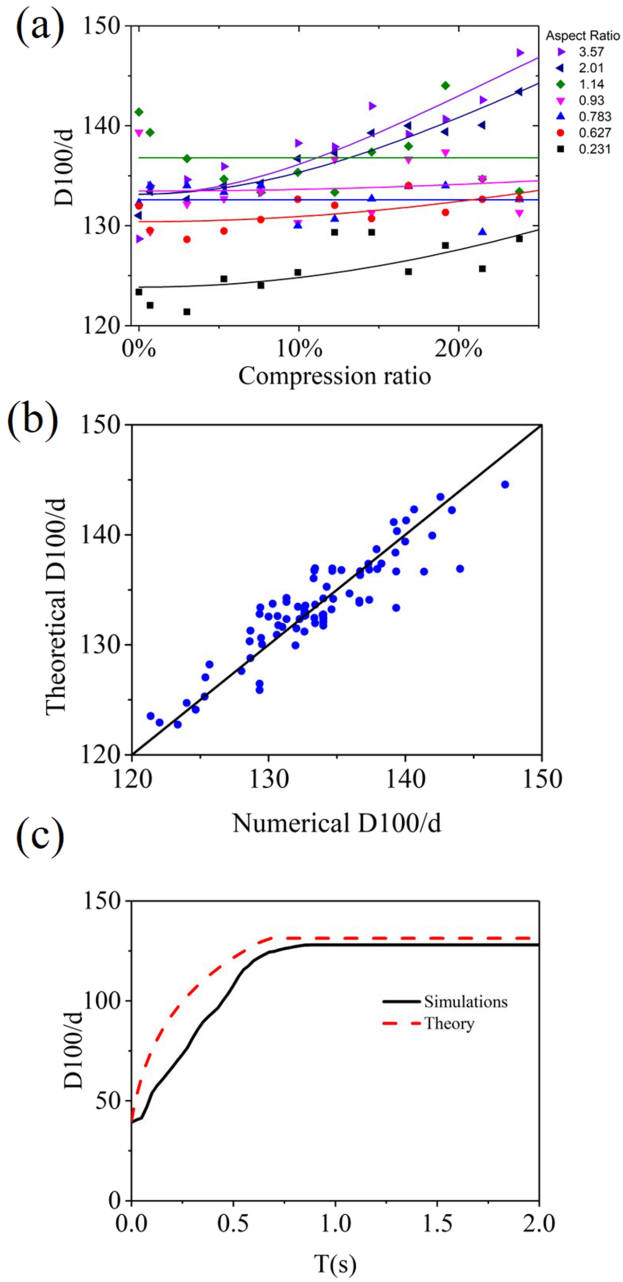

FIG. 11. (a) Numerical simulation results (data points) and theoretical model predictions (lines) of horizontal spreading D100/d as a function of compression ratio for different aspect ratios. (b) Correlation between simulation and theoretical D100/d (c) Comparison between theoretical and simulation D100/d against time for the case with aspect ratio as 3.57 and compression ratio as 0.

TABLE IV. Empirical values of E_m and U_{initial} for different aspect ratios.

Aspect ratio	$E_m(N/m)$	$U_{\text{initial}}(J)$
3.57	0.740	0.0906
2.01	0.184	0.0680
1.14	0.0000873	0.0635
0.93	0.000418	0.0464
0.783	0.000118	0.0415
0.627	0.00271	0.0328
0.231	0.0034	0.0149

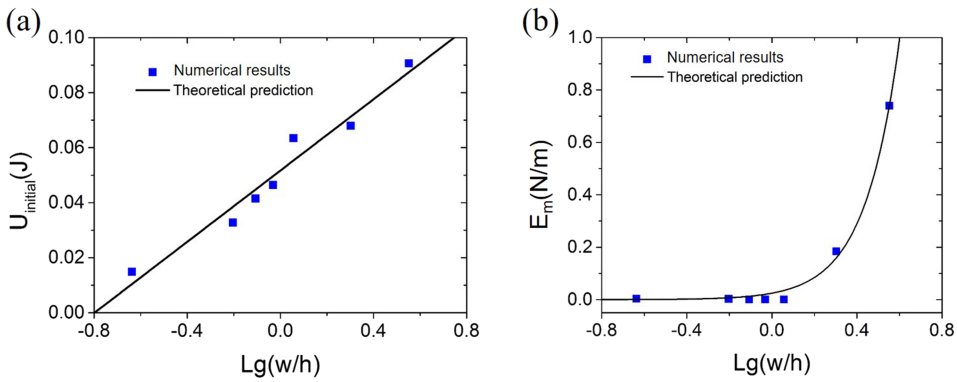

FIG. 12. Numerical simulation results (data points) and empirical fit of (a) U_{initial} and (b) E_m as a function of logarithm of the aspect ratios.

horizontal spreading D100/d against time. The theoretical and simulation results agree well. The settling time of both theoretical and simulation results are around 0.7s. The empirical values of the parameters E_m and U_{initial} obtained from fitting the simulation data with theoretical equations are shown in Table IV and plotted in Figure 12 as functions of aspect ratio.

U_{initial} increases linearly with the log of aspect ratio as shown in Figure 12a; which leads us to a linear fit for U_{initial} in terms of aspect ratio w/h:

$$U_{\text{initial}} = 0.0648 \lg\left(\frac{w}{h}\right) + 0.0517\,. \tag{25}$$

On the other hand, E_m increases exponentially with the log of aspect ratio, as shown in Figure 12b. The exponential fit is:

$$E_m = 1.58 \exp(6.16 \lg\left(\frac{w}{h}\right) - 4.16)\,. \tag{26}$$

From the theoretical framework, $D100$ is a function of both E_m and U_{initial}, so the horizontal spreading can be predicted using Equations 24, 25 and 26.

V. CONCLUSION

From our numerical simulations we made the following observations:

- The total spreading (D100) and the spreading of the bulk of the granular material (D90) are not affected the same way by the factors considered here, and thus it is not a good idea to consider just one of them as being characteristic of the overall behaviour.
- Both D100 and D90 increase as the aspect ratio (width/height) increases, especially at large compression ratios.
- D100 generally increases with compression ratio, except at aspect ratios close to 1.
- The dependence of D90 on compression ratio is complex: it tends to decrease with compression ratio at small aspect ratios, but increases with compression ratio at large aspect ratios. By considering the slopes of the linear fits of D100 and D90 as a function of compression ratio, we can

approximate a range of aspect ratios outside of which both D100 and D90 will increase with compression ratio.

- The compaction process used in the numerical simulation does not appear to have greatly significant effect on either D100 or D90; except that a smaller number of compactions and allowing the particles to settle for a longer period may result in less elastic potential energy building up in the particles directly experiencing the compaction.

The differences exhibited by D100 and D90 are likely to be a reflection of the different local concentration at the edges of the cluster of particles compared to within the cluster itself. On the edge where the local concentration is less – especially for the particles right at the edge – fluid forces would be more significant than the effects of neighbouring particles, and the particles would have more 'space' to move into. Within the cluster, particles are surrounded by their neighbours and thus the direct and indirect particle interactions would be more significant than fluid forces, and their 'free space' would be much less.

We hypothesise that the reason for the non-uniformity in the results above, whether as a function of compression ratio or aspect ratio, is likely to be because the elastic potential energy imparted to the particles during the compression is not distributed uniformly. This means that the initial velocity of the particles are non-uniform and, in turn, the responding effects of the surrounding fluid on the particles' motion (incorporated as fluid drag, added mass and Stokeslet disturbances) will also be more complex.

Since D90 represents the spreading of the bulk of the particles while D100 represents the total amount of spreading, for the purposes of reducing the amount of pollution caused in nodule harvesting the goal is to minimise D100. Based on the general observations above, we would recommend compacting the sediment tailings into a shape with low width-to-height ratio and applying a low amount of compression, before discharging underwater.

In addition, we propose a simple theoretical model for predicting the horizontal spreading (D100) as a function of both compression and aspect ratios. The model involves two new parameters E_m and $U_{initial}$, both of which are functions of aspect ratio only. The compression ratio affects the energy stored inside the bulk of particles and affects its initial velocity, which can be seen from Eq. (14). Here we use the numerical simulation results to obtain expressions for both of these parameters, and the resulting theoretical predictions of horizontal spreading compare relatively well to the data.

We note that these expressions may not be very accurate compared to reality due to various factors, for instance that these are fits of numerical simulation data, and not fits directly from physical experimental data. Another factor is that numerical simulations are only approximations of reality, and do not have the full size distribution of granular material present in the physical system. In this paper, the initial velocity of the particles at the point of discharge is set to zero, although it is non-negligible in reality. However we believe that the salient characteristics have been reproduced adequately, and thus the qualitative relationships obtained in this paper will still apply.

We recognise that this work is still very simple, given that only the compression ratio and aspect ratio were studied, and that there are many other parameters such as surface area to volume ratio or bulk solid fraction which should be included to present a more holistic picture. In terms of the granular media itself, the effects of different particle diameters and irregular shapes are also not considered here, neither are granular material that have some measure of cohesivity. There is existing research that models irregular shape particles using DEM, such as Refs. 26–28, which we can adopt and incorporate into our framework for future study. However, we believe that this paper is a good start at using external factors to optimise the amount of spreading. The theoretical model can also be improved on, in particular determination of the new parameters U_{initial} and E_m which are currently determined empirically from the numerical simulation results.

ACKNOWLEDGMENTS

The authors would like to extend their gratitude to Prof. Phan Thien Nhan and his research group for constructive feedback and discussion. This work was funded by the Singapore Ministry of Education (MOE) AcRF Grant, WBS no. R-265-000-508-133.

[1] A. F. Amos and O. A. Roels, Marine Policy 156 (1977).
[2] H. Thiel and F. Tiefsee-Umweltschutz, Deep Sea Research Part II: Topical Studies in Oceanography **48**, 3433 (2001).
[3] M. Schrope, Nature **495**, 294 (2012).
[4] B. Agarwal, P. Hu, M. Placidi, H. Santo, and J. J. Zhou, "Feasibility study on manganese nodules recovery in the clarion-clipperton zone" (2012).
[5] T. M. Shimmield, K. D. Black, J. A. Howe, D. J. Hughes, and T. Sherwin, Final Report: Independent Evaluation of Deep-Sea Mine Tailings Placement (DSTP) in PNG, Tech. Rep. 8.ACP.PNG.18-B/15 (SAMS Research Services Limited, 2010).
[6] S. Rolinski, J. Segschneider, and J. Sündermann, Deep Sea Research II **48**, 3469 (2001).
[7] H. J. Becker, B. Grupe, H. U. Oebius, and F. Liu, Deep-Sea Research II **48**, 3609 (2001).
[8] B. Grupe, H. J. Becker, and H. U. Oebius, Deep-Sea Research II **48**, 3593 (2001).
[9] H. U. Oebius, H. J. Becker, S. Rolinski, and J. A. Jankowski, Deep-Sea Research II **48**, 3453 (2001).
[10] A. Koschinsky, B. Gaye-Haake, C. Arndt, G. Maue, A. Spitzy, A. Winkler, and P. Halbach, Deep-Sea Research II **48**, 3629 (2001).
[11] L. H. Kalnejais, W. R. Martin, and M. H. Bothner, Marine Chemistry **121**, 224 (2010).
[12] J. Segschneider and J. Sündermann, Journal of Marine Systems **14**, 81 (1998).
[13] J. A. Jankowski and W. Zielke, Deep-Sea Research II **48**, 3487 (2001).
[14] R. Periáñez, Environmental Pollution **133**, 351 (2005).
[15] P. A. Cundall and O. D. Strack, Geotechnique **29**, 47 (1979).
[16] D. Wang, D. Ho-Minh, and D. S. Tan, The European Physical Journal E **39**, 112 (2016).
[17] K. Hill and D. S. Tan, Journal of Fluid Mechanics **756**, 54 (2014).
[18] R. Di Felice, International Journal of Multiphase Flow **20**, 153 (1994).
[19] T. Auton, J. Hunt, and M. Prud'Homme, Journal of Fluid Mechanics **197**, 241 (1988).
[20] Z. Jiang and P. Haff, Water Resources Research **29**, 399 (1993).
[21] T. G. Drake and J. Calantoni, Journal of Geophysical Research: Oceans (1978–2012) **106**, 19859 (2001).
[22] J. Calantoni, K. T. Holland, and T. G. Drake, Philosophical Transactions-Royal Society of London Series a Mathematical Physical and Engineering Sciences **362**, 1987 (2004).
[23] J. Nitsche and G. Batchelor, Journal of Fluid Mechanics **340**, 161 (1997).
[24] B. Metzger, M. Nicolas, and E. Guazzelli, Journal of Fluid Mechanics **580**, 283 (2007).
[25] D. Tan and S. Ng, in *Proceedings of the 20th Australasian Fluid Mechanics Conference (20AFMC), Perth, Australia* (2016), p. 437.
[26] R. Gao, X. Du, Y. Zeng, Y. Li, and J. Yan, Journal of Rock Mechanics and Geotechnical Engineering **4**, 276 (2012).
[27] T. Matsushima, H. Saomoto, M. Matsumoto, K. Toda, and Y. Yamada, in *16th ASCE engineering mechanics conference* (American Society of CIvil Engineers, 2003).
[28] F. Radjaï and F. Dubois, *Discrete-element modeling of granular materials* (Wiley-Iste, 2011).